

# **SuperDTI: Ultrafast diffusion tensor imaging and fiber tractography with deep learning**

Hongyu Li<sup>1</sup>, Zifei Liang<sup>2</sup>, Chaoyi Zhang<sup>1</sup>, Ruiying Liu<sup>1</sup>, Jing Li<sup>3</sup>, Weihong Zhang<sup>3</sup>, Dong Liang<sup>4</sup>, Bowen Shen<sup>5</sup>, Xiaoliang Zhang<sup>1</sup>, Yulin Ge<sup>2</sup>, Jiangyang Zhang<sup>2</sup>, Leslie Ying<sup>1,6</sup>

<sup>1</sup>Electrical Engineering, University at Buffalo, State University of New York, Buffalo, NY, USA

<sup>2</sup>Center for Biomedical Imaging, Radiology, New York University School of Medicine, New York, USA

<sup>3</sup>Radiology, Peking Union Medical College Hospital, Peking Union Medical College and Chinese Academy of Medical Sciences, Beijing, China

<sup>4</sup>Paul C. Lauterbur Research Center for Biomedical Imaging, Medical AI research center, SIAT, CAS, Shenzhen, P.R.China

<sup>5</sup>Computer Science, Virginia Tech, Blacksburg, VA, USA

<sup>6</sup>Biomedical Engineering, University at Buffalo, State University at New York, Buffalo, NY, USA

## **Correspondence**

Leslie Ying, Ph.D.

Department of Biomedical Engineering, Department of Electrical Engineering, University at Buffalo, State University of New York

223 Davis Hall, Buffalo, NY, 14260, USA

Email: leiying@buffalo.edu

**Purpose:** To propose a deep learning-based reconstruction framework for ultrafast and robust diffusion tensor imaging and fiber tractography.

**Methods:** We propose SuperDTI to learn the nonlinear relationship between diffusion-weighted images (DWIs) (reduced in q-space and k-space) and the corresponding tensor-derived quantitative maps as well as the fiber tractography. Super DTI bypasses the tensor fitting procedure, which is well known to be highly susceptible to noise and artifacts in DWIs. The network is trained and tested using datasets from Human Connectome Project and patients with ischemic stroke. The noise robustness of the network and the lesion detectability of the reconstructed maps are evaluated. SuperDTI is compared against the state-of-the-art methods for diffusion map reconstruction and fiber tracking.

**Results:** The proposed technique is able to generate fractional anisotropy and mean diffusivity maps, as well as fiber tractography, from as few as six undersampled raw DWIs. SuperDTI achieves a quantification error of less than 5% in all regions of interest in white matter and gray matter structures. In addition, we demonstrate that the trained neural network is robust to additional noise in the testing data, and the network trained using healthy volunteer data can be directly applied to stroke patient data without compromising the lesion detectability.

**Conclusion:** This paper demonstrates the feasibility of superfast diffusion tensor imaging and fiber tractography using deep learning with as few as six corrupted DWIs (up to 30-fold). Such a significant reduction in scan time will allow the inclusion of DTI into clinical routine for many potential applications.

## **KEYWORDS**

Diffusion tensor imaging (DTI), fast DTI, fiber tractography, lesion detectability, deep learning, convolutional neural network

## 1. INTRODUCTION

Diffusion-weighted imaging (DWI) uses diffusion sensitizing gradients to measure the extent of water molecule diffusion along the gradient direction (1-3). DWI has shown to be useful for early detection of ischemic stroke (1,4), as well as other brain diseases, such as multiple sclerosis (5-7), trauma (8,9), brain tumors (10,11), and hypertensive encephalopathy (12,13). To account for complex patterns of water diffusion profiles shaped by tissue microstructural organization, e.g., anisotropic diffusion in white matter structures, diffusion tensor imaging (DTI) was later developed to characterize three-dimensional tissue water diffusion using a second-order diffusion tensor model (14). From DTI data, several markers, such as mean diffusivity (MD) and fractional anisotropy (FA), can be derived and are widely used to visualize microstructural organizations in the brain as the diffusion tensor itself, a three-by-three matrix, is difficult to visualize. Furthermore, the 3D directional anisotropy information encoded in diffusion tensors allows non-invasive reconstruction of the trajectories of major white matter tracts in the brain (15). Although more sophisticated diffusion MRI techniques, such as diffusion kurtosis imaging (16) and high angular resolution diffusion imaging (HARDI) (17), have been developed to provide more comprehensive information on tissue microstructure (e.g., non-Gaussian diffusion and fiber crossing), DTI remains an important tool for neuroscience research with a wide array of clinical applications.

Although DTI theoretically requires only six diffusion-weighted images and one non-diffusion-weighted image for estimation of the diffusion tensors, a large number of diffusion-weighted images with different diffusion encoding directions are often acquired in practice due to the low SNR and high sensitivity of the tensor model to noise contamination. For example, 30-90 DWIs are typically needed to obtain MDs and FAs with diagnostic quality, resulting in a scan time of 10-30 minutes. Such a prolonged scan time can increase motion artifacts and the patient's discomfort. Several techniques have been developed to accelerate DTI, such as parallel imaging based simultaneous multislice (SMS) acquisition (18), and compressed sensing (19-24). However, the

acceleration factor is limited to 2-3, with the latter involving extensive computation power.

Here we report a deep learning approach to shorten the acquisition time of DTI dramatically. This approach can be applied on top of SMS and requires little online computation once the training is completed offline. We used deep convolutional neural networks to model the nonlinear relationship between the acquired DWIs (noisy and might be corrupted due to k-space undersampling) and the desired DTI-derived maps, and the speed improvement was achieved by reducing the number of DWIs and the amount of k-space data of each DWI at the same time. Although machine learning has been used to accelerate diffusion MRI (25,26), at least 12 DWIs were needed to generate DKI and NODDI-derived maps (25) and 25 DWIs for fiber tracking (26). In (25), a multi-layer perceptron (MLP) network (called q-space deep learning (q-DL) here) was used to learn various diffusion parameters from the q-space samples at each pixel without imposing diffusion models. The q-DL and other subsequent studies have demonstrated the potential of using machine learning to reduce the q-space data necessary for diffusion image (27-32). Besides multi-layer perceptrons (25,27,31), some used convolutional neural networks (26,28-30,32,33). The recent DeepDTI method used a convolutional neural network to improve the low quality DWIs before the DWIs are fitted to the tensor model (34). Such a ‘denoising’ network also demonstrated the feasibility of fast DTI using deep learning.

In this study, we develop a deep convolutional neural network to generate FA/MD, directionally encoded colormaps, and fiber tractography using as few as 6 DWIs. These DWIs can be noisy and/or even corrupted by aliasing artifacts. We name our approach SuperDTI. Some of the preliminary results have been reported in conference abstracts (29,30). SuperDTI is different from q-DL and its derivatives in that a novel residual-learning convolutional neural network is designed to generate the quantitative maps directly from the entire DWIs (instead of pixel-wise calculation in (25)) such that the correlation in image domain and q-space are both utilized. As a result, we demonstrate the feasibility of highly accelerated (up to 30× acceleration) DTI and fiber tracking using

our proposed SuperDTI method, bypassing all models. Our results show that as few as 6 raw DWIs, each undersampled by a factor of 2, are needed to for FA maps and fiber tractography, and 3 raw undersampled DWIs for MD maps. Furthermore, we show that the learned networks is robust to additional noise in DWIs, and also verify that networks trained using healthy subjects can potentially be applied to stroke patients with lesions.

## 2. THEORY

### 2.1 Network architecture

Our objective is to represent the nonlinear mapping between  $q$  DWIs (input) and the FA, MD or FA color maps (output) using a deep neural network, bypassing the tensor fitting process. If the nonlinear mapping between the input  $x$  and the output  $y$  is represented as  $y = F(x; \Theta)$ , where  $\Theta$  is the parameter that controls the nonlinear relationship, then a deep neural network is designed such that the parameter  $\Theta$  can be learned to represent the true relationship through training. Figure 1 shows the basic architecture of the convolutional neural network (CNN) used in SuperDTI. In the deep learning method, CNN uses an input layer, an output layer, and multiple hidden layers of nodes to form a hierarchical structure. Each node of a layer is connected to some nodes of the previous layer by a linear convolution, a nonlinear activation, or a pooling (reduction from multiple to one) process. Such a hierarchical structure with deep layers can represent highly complex nonlinear models, with different network parameters representing different models.

SuperDTI is a deep U-net (35) style encoder-decoder network with residual learning (36) and patch-wise training/padding (37,38). The skip connection, originally introduced in ResNet (36), copies the feature maps from early convolutional layers and reuses them as the input to later deconvolutional layers of the same size in a network. There are four conveying paths in our networks which enable residual learning to boost CNN performance (36). Except for the last layer, each convolutional or deconvolutional layer is followed by a rectified linear unit (ReLU).

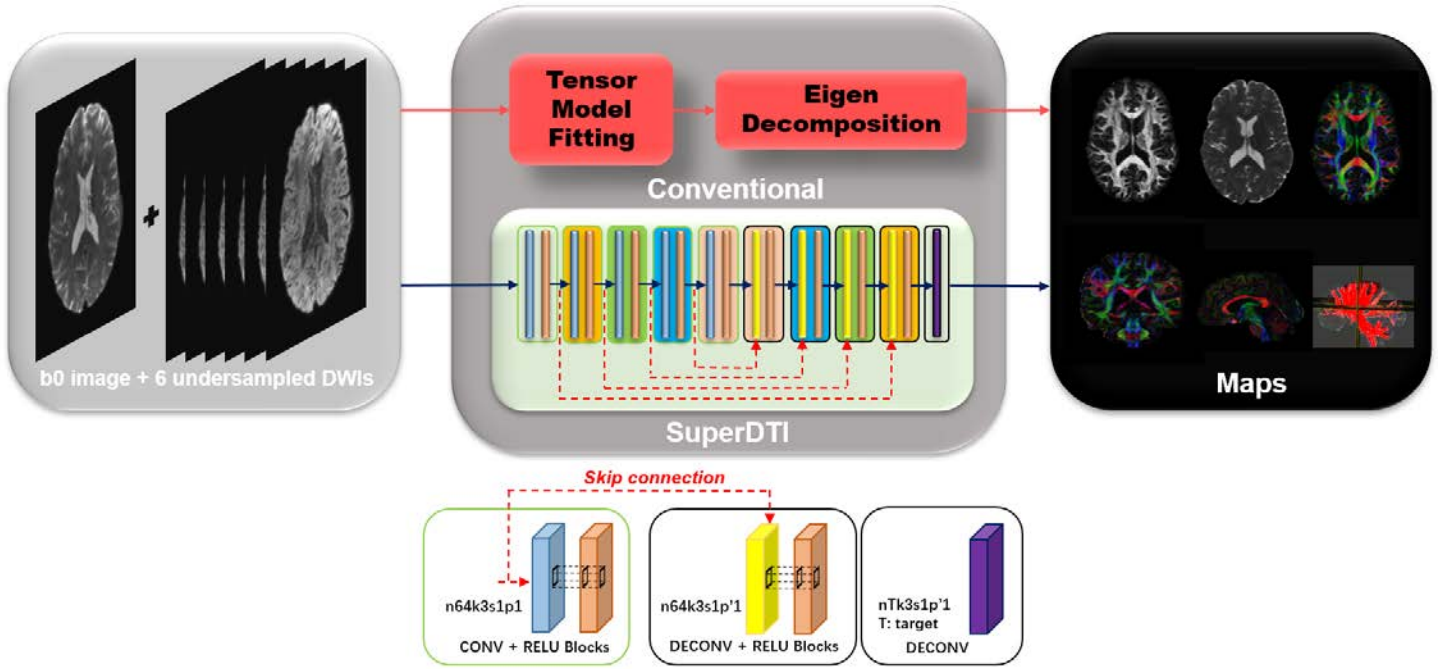


**FIGURE 1** Schematic comparison of the conventional DTI model fitting and deep learning methods SuperDTI for generating various diffusion quantification maps. The proposed network comprises several layers of a skip-connection-based convolution-deconvolution network which learns the residual between its input and output. In each layer,  $n64k3s1p1$  ( $p'1$ ) indicates 64 filters of kernel size  $3 \times 3$  with a stride of 1 and padding of 1 (truncation of 1). Except for the last layer, each (de)convolutional layer is followed by a ReLU unit.

We use a  $L$  layers (de)convolutional neural network architecture. Specifically, each of the  $l = 1, \dots, L$  hidden layers calculates

$$H_l = \sigma_l(W_l * H_{l-1} + B_l) \quad (1)$$

for layers without skip connection, and

$$H_l = \sigma_l(W_l * (H_{l-1} + H_{L-l}) + B_l) \quad (2)$$

for layers with skip connection, where  $H_l$  is the output of layer  $l$  ( $H_0$  stands for input),  $W_l$  and  $B_l$  represent the filters and biases respectively, ‘\*’ denotes the (de)convolution operation, and  $\sigma_l$  the nonlinear operator (e.g., ReLU is used here). Here,  $W_l$  corresponds to  $n_l$  filters of support  $n_{l-1} \times c \times c$ , where  $n_{l-1}$  is the number of channels in the previous layer,  $c$  is the spatial size of a filter.

## 2.2 Network training

In our training, we opted to use patch-wise images instead of the original images as input. The patch processing

cropped the original images into  $21 \times 21$  overlapping patches. The reason we used patch-wise processing is explained as follows. During network training, the memory of a single batch is limited. If we directly feed the original images into the training, the network can only take limited images in one batch because of memory overflow. Alternatively, if we divide the image into many overlapping patches and shuffle them, we will be able to provide abundant training data in a single batch and prevent overfitting, as seen in many deep learning studies (37,38). By using overlapping patches, we generated approximately 16,000,000 training samples from 40 HCP datasets.

During training, both the input (DWIs) and output (ground truth FA, MD or Eigenvectors) are given. The information is then used to train the filter weights and biases. Specifically, the objective is to minimize the loss function defined as the average mean squared error (L2) between the network prediction of input  $x^t$  and the corresponding ground truth result  $y^t$  for all training samples  $t = 1, \dots, n$ :

$$L(\theta) = \frac{1}{n} \sum_{t=1}^n \|F(x^t; \theta) - y^t\|^2, \quad (3)$$

where  $F(\cdot)$  represents the operation performed by the neural network, and  $\theta$  denotes the filter weights  $W_l$  and biases  $B_l$ . For multi-channel tasks (Eigen-vectors), the cost function is the averaged loss of all channels. The optimization problem is solved by the backpropagation algorithm implemented in Caffe (39).

### 3. METHODS

#### 3.1 Data acquisition

##### **Human connectome project data**

DWI data from a total of 50 subjects were randomly selected from the Human Connectome Project (HCP Young Adult) (40). The diffusion-weighted scans were performed using an HCP-specific variant of the multiband diffusion sequence. The diffusion MRI data were collected with 3 different gradient tables, each including 90

diffusion weighting directions, plus six  $b = 0$  acquisitions. The diffusion directions were uniformly distributed on multiple q-space shells. The directions were optimized so that every subset of the first  $M$  directions is also isotropic. Each dataset includes 18 non-DWIs and 270 DWIs in three different b values: 1000, 2000, and 3000  $\text{s/mm}^2$  and 90 diffusion directions. Data from 40 subjects (145 slices for each subject, a total of 5,800 images) were used for training, and the data from the rest 10 subjects were used for testing and statistical analysis.

### **Healthy volunteer and stroke patient data**

The data used in this study were acquired previously in an ongoing trial (Identifier: NCT03163758) as described in (41,42). The study was approved by the ethics committee of the Peking Union Medical College Hospital. We selected data from 10 healthy volunteers (5 males and 5 females, age  $54.4 \pm 7.8$  years) and 2 stroke patients (30 and 76 years old). MRI data including DWIs and structural images were acquired on a 3.0T MRI scanner (MAGNETOM Skyra; Siemens, Erlangen, Germany) using a 20-channel phased-array head coil. The DWI images were acquired with a diffusion-weighted echo-planar imaging sequence (EPI) sequence. The DWI scan consisted of 30 diffusion-weighted directions with a b-value of  $1000 \text{ s/mm}^2$  and one volume without diffusion weighting (i.e.,  $b_0$  image). The parameters of the DTI sequence were as follows: repetition time (TR) = 7900 ms, echo time (TE) = 94 ms, slice thickness = 2.5 mm, field of view (FOV) =  $240 \text{ mm} \times 240 \text{ mm}$ , 60 axial slices with a slice thickness of 2.5 mm, slice gap 0.5 mm, matrix size =  $122 \times 122$ , and two repetitions. Earplugs and earphones were used to reduce scan noises, and the head motion was minimized by stabilizing the head with cushions. Based on the acquisition protocol of this data, the selected  $M = 6, 8, \text{ or } 10$  diffusion directions were uniformly distributed on the q-space shell with  $b = 1000 \text{ s/mm}^2$ . Data from 10 healthy volunteers (a total of 600 images) were used for training and validation, and the data from the 2 stroke patients were used for testing and analysis.

### **3.2 Data processing**



The model-fitting results from all 90 directions of  $b=1000 \text{ s/mm}^2$  were used as the reference for training of the deep learning network, calculation of statistical metrics, and comparison of performance. A subset of the DWIs were chosen to generate the desired maps using both the proposed and state-of-art methods. Based on the acquisition protocol of the HCP data, the first  $M = 6, 18, \text{ or } 36$  diffusion directions were selected such that they are uniformly distributed on the q-space shell with  $b = 1000 \text{ s/mm}^2$ . Such a uniform selection of the diffusion-encoding scheme improves both the rotational invariance of measurement precision and the robustness to noise (43). MRtrix (44) was used to perform the conventional model fitting (MF) using the diffusion tensor model. Conventional MF, MLP (similar to (25) but for DTI), and BM4D (45,46) denoising followed by MF were used for comparison. DtiStudio (47) was used for generating fiber tractography. All testing images were segmented into 286 regions of interest (ROIs) using a multiple-atlas likelihood fusion algorithm (48). The mean values and errors in each ROI were calculated. The performance of different methods in representative gray matter, major white matter, and subcortical white matter structures were examined.

The entire dataset was normalized to a constant value defined by the maximum intensity of the dataset. In addition, data augmentation (rotating and flipping) is used. Among the training dataset for all experiments, 20% of them were used as validation, and the testing data were strictly excluded from the training part.

### **3.3 Evaluation metrics**

Peak signal-to-noise ratio (PSNR), normalized mean squared error (NMSE) and structural similarity index (SSIM) (49) were used to quantify the similarity between the results of different methods compared to the reference. The lesion contrast was calculated as the FA value difference between the lesion and the surrounding background normalized by the mean FA value of the background. Large values suggest better contrasts.

## 4. RESULTS

### 4.1 FA and MD maps

The network in Figure 1 was trained (on 40 subjects) and tested (on 10 other subjects, i.e.,  $n = 10$ ) using the diffusion data from the HCP dataset. Figure 2 shows representative FA maps from 6 DWIs generated using the conventional tensor model fitting (MF), multi-layer perceptron (MLP) (similar to (25)), block-matching and 4D filtering (BM4D) denoising algorithm (45,46), the proposed deep learning method (SuperDTI), and the proposed deep learning method with  $2\times$  k-space undersampling (SuperDTI+). Figure 3 plots the average mean values and the NMSEs for FA at several ROIs in gray matter structures, subcortical, and major white matter structures for all 10 testing datasets. Figure 4 shows representative MD maps from 3 DWIs using different methods. Results from MF using all 90 DWIs plus 18 non-weighted images were used as the ground truth. While other results became noisy or blurry in such an extreme case, the FA maps generated by our proposed method showed no apparent degradation. The generated FA/MD maps were quantitatively evaluated using the PSNRs, SSIMs, and NMSEs, which show good performance for SuperDTI even with only 6 DWIs for FA and 3 DWIs for MD maps. It is seen that the difference between the MD maps is far less apparent than that between the FA maps. This is because the MD calculation is less sensitive to noise.

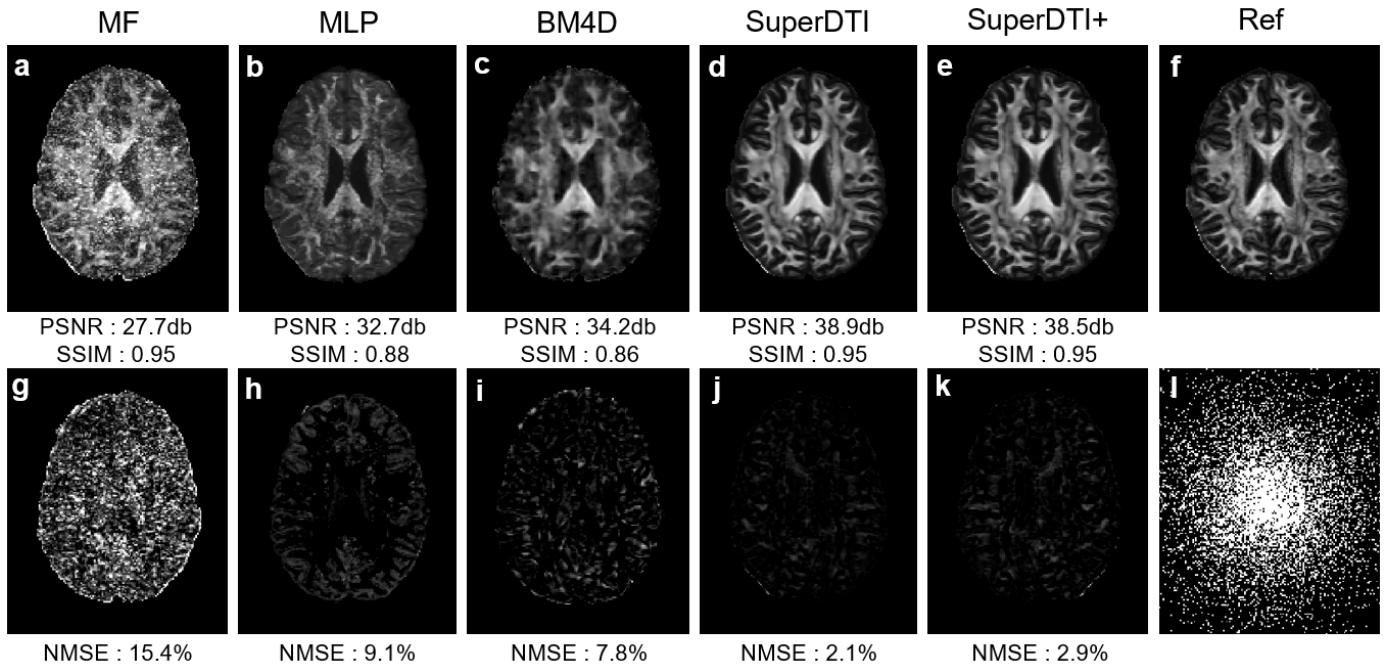


**FIGURE 2** Comparison of FA maps generated from 6 DWIs using different methods. FA maps generated by (a) MF, (b) MLP, (c) BM4D, (d) proposed SuperDTI, (e) proposed SuperDTI+ with additional 2x k-space undersampling (the variable-density pseudo-random sampling pattern is shown in (l)), and (g)-(k) the corresponding error maps respectively. The PSNRs, SSIMs, NMSEs, and error maps were calculated with (f) the model fitted FA map from 90 DWIs as the reference.

Within ROIs defined in the cortical gray matters, subcortical, and major white matter structures, the FA values estimated from limited DWIs using the proposed method also showed significantly less deviation from the ground truth than other methods. When only 6 DWIs were available, the conventional MF method significantly overestimated the FA values, whereas the SuperDTI had NMSEs below 3.5% for GM structures, below 1.5% for subcortical WM structures, and below 4% for major WM structures.

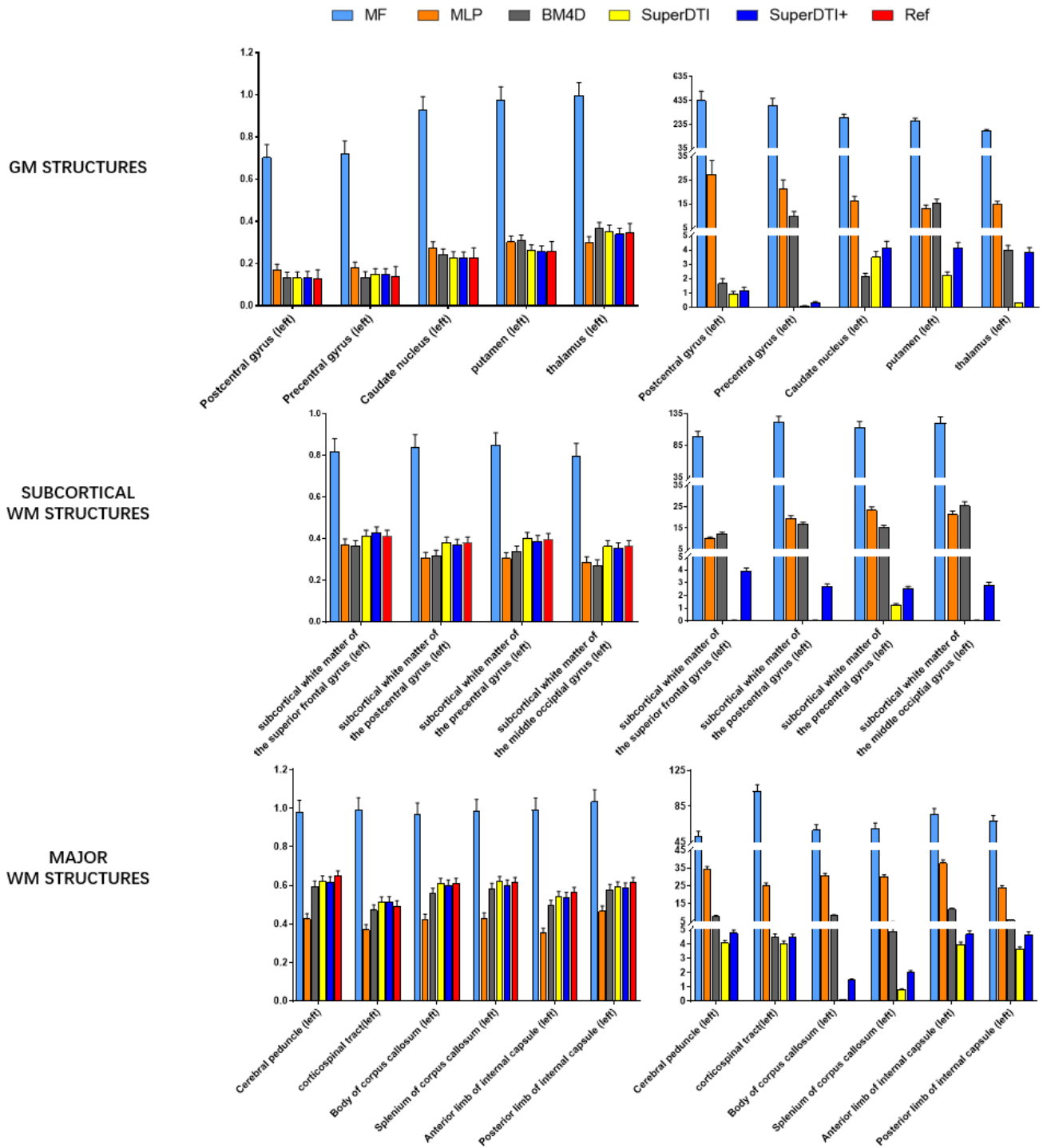


**FIGURE 3** Comparison of mean FA values (left) and the corresponding percentage error (right). Values and errors were obtained by MF, MLP, BM4D, SuperDTI, SuperDTI+ with 6 DWIs for different ROIs.

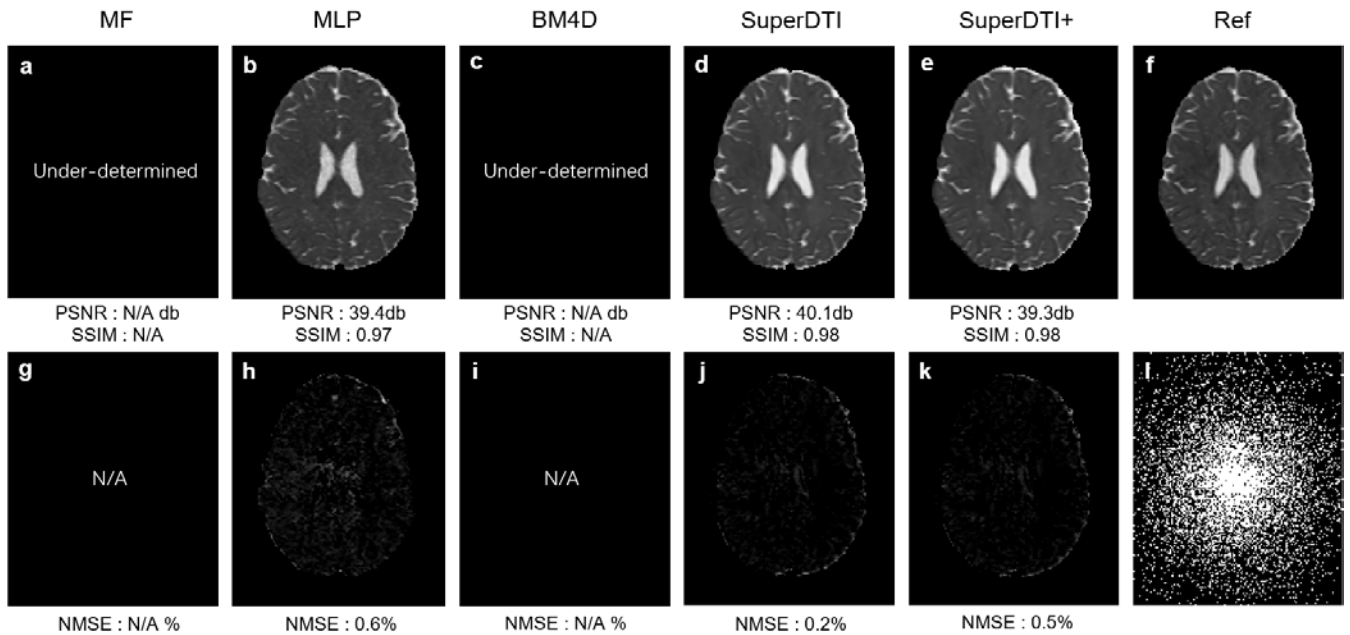


**FIGURE 4** Comparison of MD maps generated from 3 DWIs using different methods. MD maps generated by (a) MF, (b) MLP, (c) BM4D, (d) proposed SuperDTI, (e) proposed SuperDTI+ with additional 2x k-space undersampling (the variable-density pseudo-random sampling pattern is shown in (l)), and (g)-(k) the corresponding error maps respectively. The PSNRs, SSIMs, NMSEs, and error maps were calculated with (f) the model fitted FA map from 90 DWIs as the reference.

## 4.2 Directionally encoded colormap and fiber tracking

The primary eigenvector from a diffusion tensor indicates the principle orientation of water molecule diffusion. The primary eigenvector can be used to generate directionally encoded colormap, which is useful to inspect 3D orientation information encoded in diffusion tensors, as well as for fiber tracking. Our DL network can also be trained to estimate the primary eigenvectors directly from DWIs without MF. Figures 5 shows the directionally encoded colormap generated from the eigenvectors using the proposed and other competing methods with 6 DWIs. Visually, the directionally encoded colormaps generated using SuperDTI and SuperDTI+ maintain the quality better than others with a small number of DWIs. Even with only 6 DWIs, the estimated orientation of the corpus callosum remains consistently along the medial-lateral orientation (5) in SuperDTI, whereas other results show more speckles due to erroneous estimates. In Figure 6, fiber tracking results using the proposed method better preserve the morphology of three major white matter tracts in the brain than the others in the extreme 6 DWIs

situation.

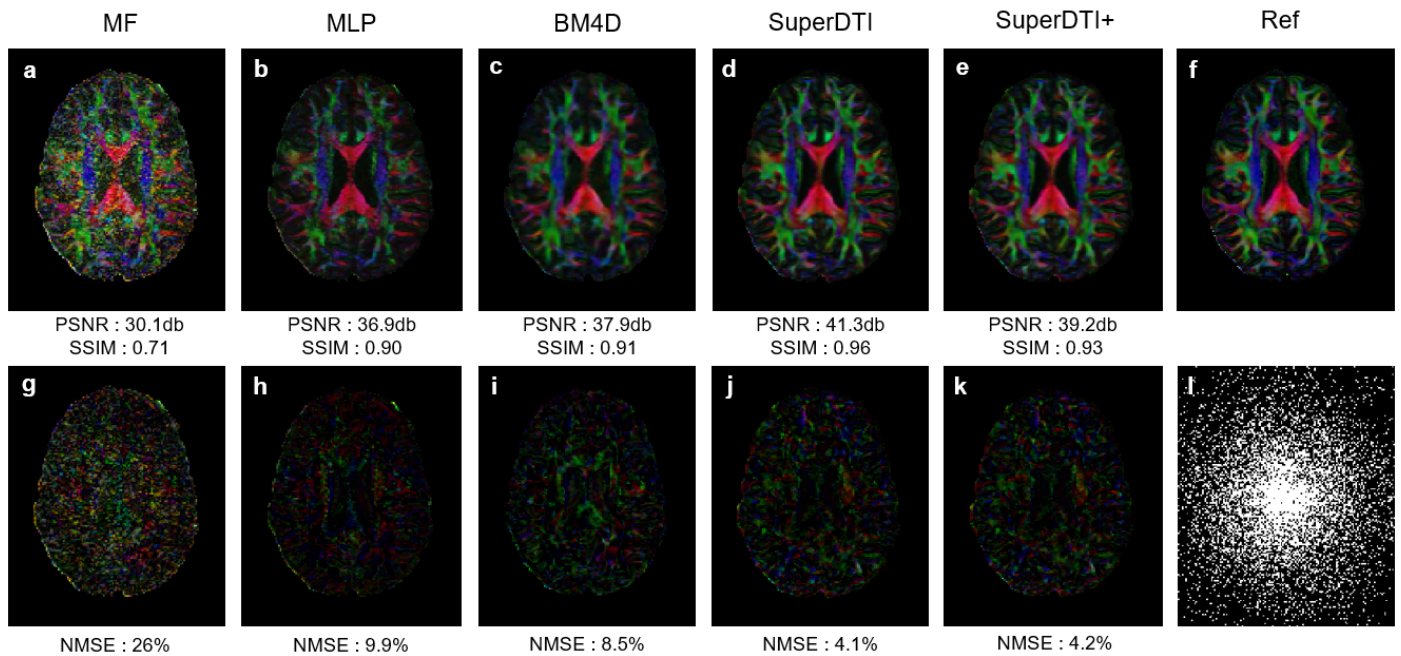


**FIGURE 5** Comparison of color-coded FA maps generated from 6 DWIs using different methods. The color maps generated by (a) MF, (b) MLP, (c) BM4D, (d) proposed SuperDTI, (e) proposed SuperDTI+ with additional 2x k-space undersampling (the variable-density pseudo-random sampling pattern is shown in (l)), and (g)-(k) the corresponding error maps respectively. The PSNRs, SSIMs, NMSEs, and error maps were calculated with (f) the model fitted colormap from 90 DWIs as the reference and shown with the average of all 3 color channels.

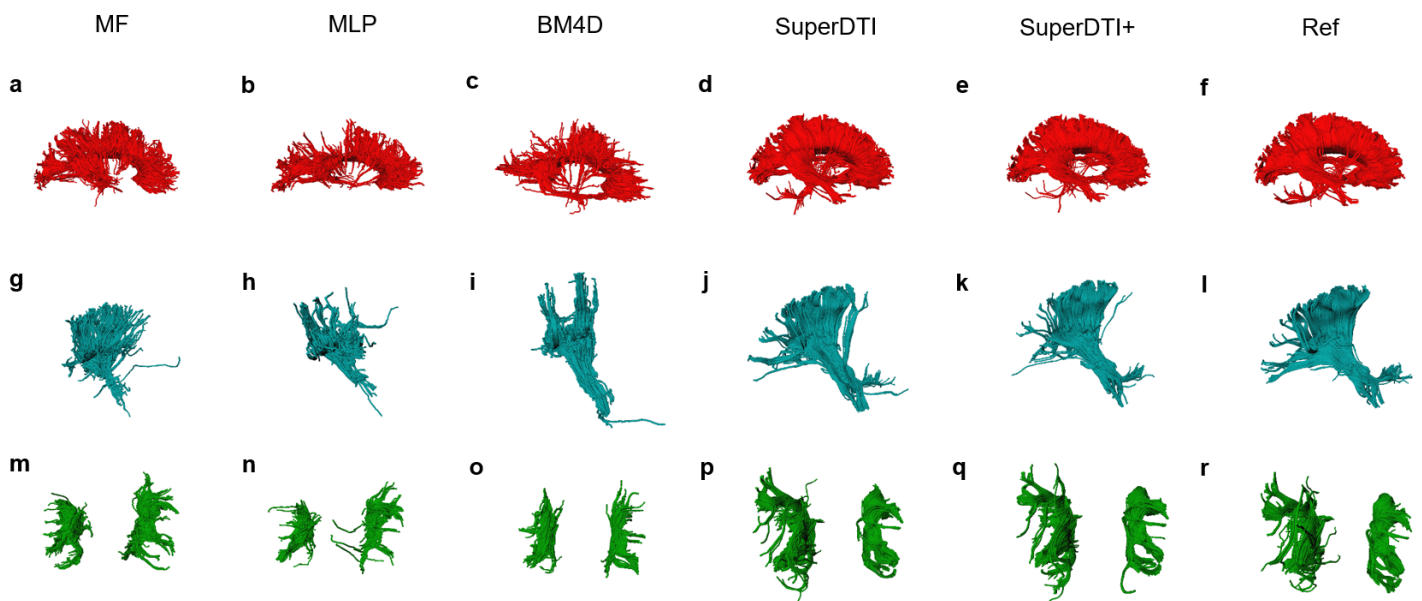


**FIGURE 6** Comparison of fiber tractography generated from 6 DWIs using different methods. Corpus callosum, internal capsule/corticospinal tract, and superior longitudinal fasciculus generated by MF (a, g, m), MLP (b, h, n), BM4D (c, i, o),

SuperDTI (d, j, p), and SuperDTI+ (e, k, q) with  $2\times$  k-space undersampling, respectively. Tractography from 90 DWIs (f, l, r) is shown as the reference.

### 4.3 Statistical analyses

For the HCP data, ten sets of test images (a total of 1450 images) were used to evaluate the statistical accuracy of the FA, MD, and directionally encoded FA colormap values estimated using different methods. Quantitative assessments of PSNRs, NMSEs, and SSIMs are summarized in Table 1.

**TABLE 1** Quantitative Assessment of FA, MD, and FA colormap using different methods

Methods			MF	MLP	BM4D	SuperDTI	SuperDTI+
FA	6 DWIs	PSNR	27.15	32.89	33.96	38.60	38.29
		NMSE	0.17	0.09	0.08	0.02	0.03
		SSIM	0.69	0.88	0.85	0.95	0.95
MD	3 DWIs	PSNR	N/A	37.97	N/A	38.61	38.36
		NMSE	N/A	0.007	N/A	0.002	0.006
		SSIM	N/A	0.97	N/A	0.98	0.97
Color	6 DWIs	PSNR	30.12	36.95	37.93	41.34	39.28
		NMSE	0.26	0.09	0.08	0.04	0.04
		SSIM	0.71	0.90	0.91	0.95	0.93

### 4.4 Robustness to noise

In order to study the robustness to noise, we added additional 30db Rician noise to the diffusion-weighted images.

As shown in Figure 7(g), the result shows that the conventional model fitting method fails to generate acceptable

FA maps, even using all 90 DWIs. In contrast, our proposed method is still capable of generating accurate maps

using as few as 6 noisy DWIs, regardless if the neural network is trained using noisy or clean DWIs.

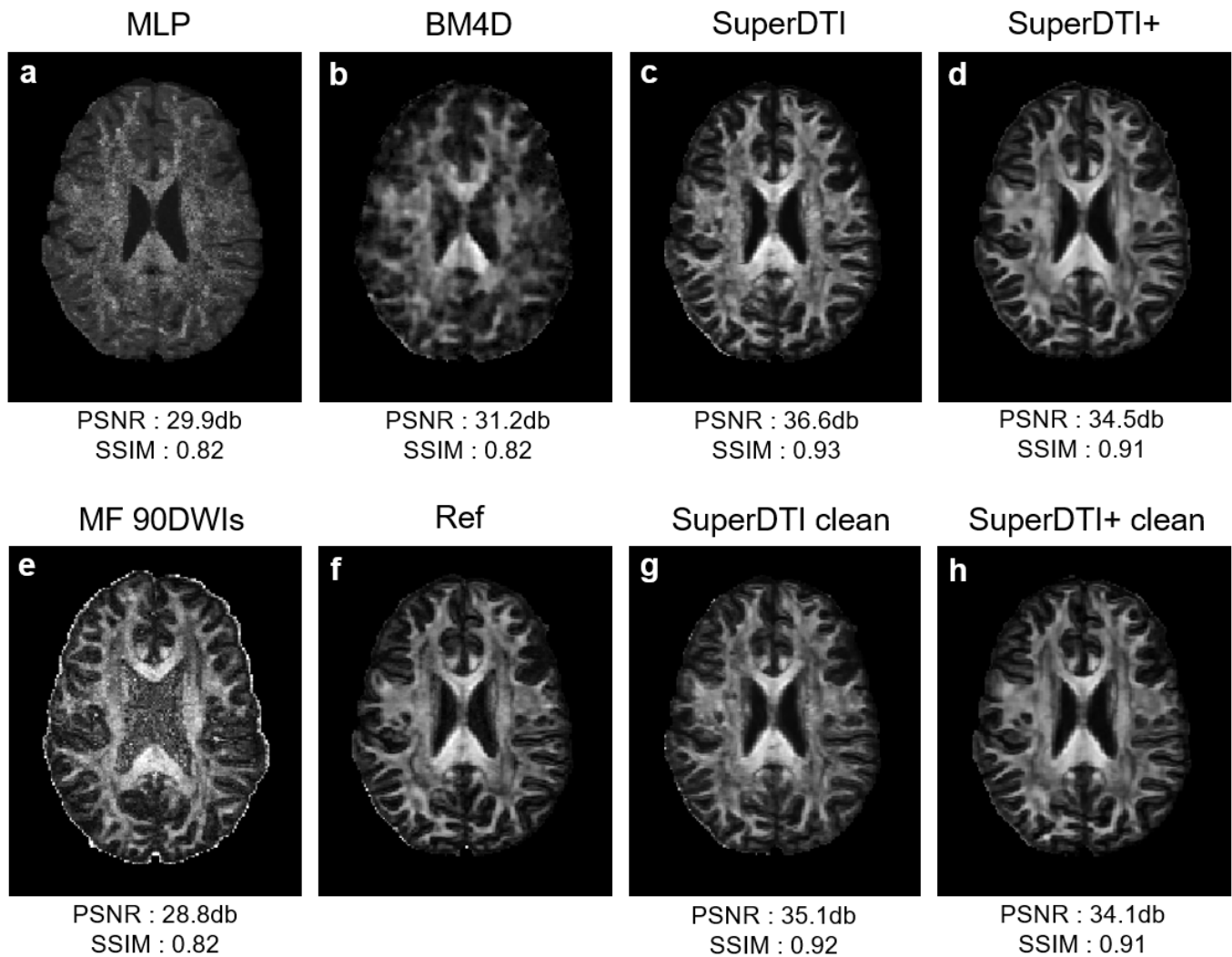


**FIGURE 7** Comparison of FA maps generated with noisy DWIs. FA maps generated from 6 noisy DWIs by (a) MLP, (b) BM4D, (c) proposed SuperDTI, (d) proposed SuperDTI+ with additional 2x k-space undersampling. (e)(f) FA maps generated using MF from 90 noisy and clean DWIs, respectively. Noisy DWIs were used for training in (a)(c) and (d). The SuperDTI clean (g) and SuperDTI+ clean (h) denotes clean inputs for training, and they are both generated from 6 noisy DWIs. The PSNRs and SSIMs were calculated with the model fitted FA map from 90 DWIs (f) as the reference.

#### 4.5 Lesion detection in stroke patients

The proposed SuperDTI trained on 10 healthy volunteers was used to obtain the FA maps of two stroke patients. Figure 8 compares the FA maps obtained from 6, 8, and 10 DWIs using the proposed SuperDTI method with the FA map from 60 DWIs (30 directions with 2 averages) using the conventional tensor fitting as the reference. The relative contrast of the lesion is shown at the bottom of each image. It is seen that the FA map from 6 DWIs using SuperDTI can still reveal lesion with high contrast similar to that from 60 DWIs. Although the training was



performed on healthy volunteer data, the network was still able to reveal the lesion information for stroke patients.

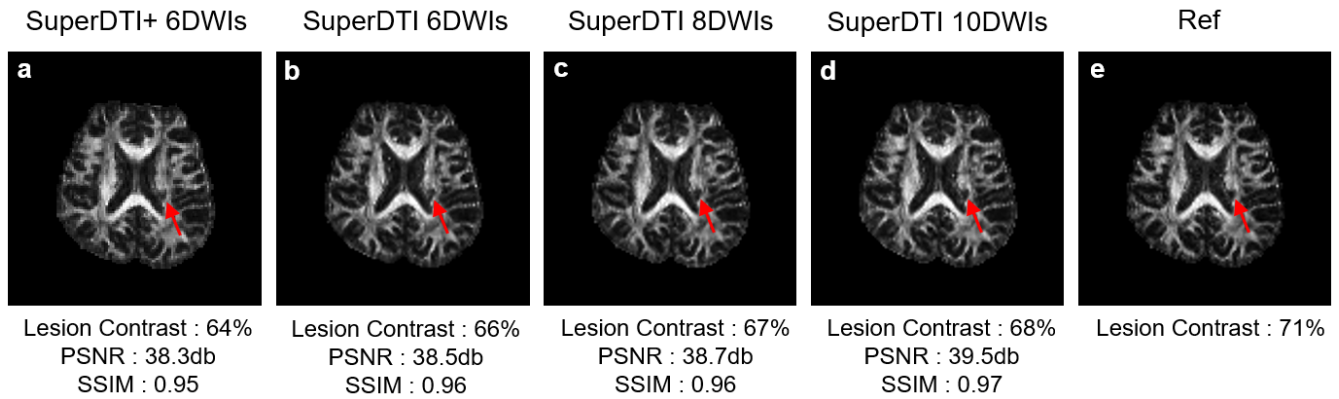


**FIGURE 8** Lesion detection using FA maps generated using SuperDTI. FA maps with a lesion (red arrow) generated by (a) SuperDTI+ and (b) SuperDTI with 6 DWIs, (c) 8 DWIs, and (d) 10 DWIs. The PSNRs and SSIMs were calculated with (e) the model fitted FA map from 60 DWIs as the reference. The lesion contrasts were calculated for all images.

#### 4.6 Effect of training size

**TABLE 2** Analysis of FA estimated by SuperDTI with different training sizes

# datasets		40 sets	20 sets	10 sets	8 sets	6 sets	4 sets	2 sets
FA	PSNR	39.3	38.9	39.2	38.6	39.0	38.2	36.7
	SSIM	0.95	0.95	0.95	0.94	0.95	0.94	0.90

We decreased the number of training datasets gradually and evaluated the accuracy of the FA values estimated by the proposed SuperDTI with 6 DWIs. The averaged NMSEs and PSNRs over all 10 testing datasets were summarized in Table 2. It can be seen that both NMSEs and PSNRs stay about the same as the training size decreases until only 2 datasets were used for training. This demonstrates that by using overlapping patches for training, sufficient training data were used in our study without overfitting.

## 5. DISCUSSION

Although deep CNN has often been treated as a black box, it is important to understand how CNN works for a specific application. For example, the training size needs to be sufficiently large to avoid overfitting. For problems with global correspondence between the input and output (e.g., image classification where the output depends on all pixels of the input image), it is common to have tens of thousands of training datasets that contain various representations of such global correspondence. For problems with local correspondence (e.g., voxel-wise fitting of image intensities to a specific model (50)), significantly fewer training datasets are required. The results in Table 2 indicate that the proposed network does not need many training sets. This is because the values on the DWIs and those on the quantitative maps are local correspondence (theoretically pixel-wise correspondence). Each image already has a large number of pixels, which provide a large number of training sets. As a result, only a few images are needed for training the proposed network. Although it is always a challenge to predict the minimum training size required, the 5800 training images used in this study were shown empirically to be sufficient to ensure robustness and avoid overfitting of the proposed network. The reason we choose CNN over MLP is that MLP has the characteristic of fully connected layers, where each node is connected with every node in the adjacent layer. As a result, the total number of trainable parameters in MLP can grow exponentially. In contrast, CNN is more much efficient by taking advantage of the spatial correlation in image pixels.

Another critical issue is whether the network trained using a set of data can be generalized to a separate set of data. Our results in Figure 8 demonstrate that the proposed SuperDTI preserves the ability to detect lesions even though the network was trained using data from normal subjects. This ability can be explained by the local relationship between DWIs and FA maps. Since FA values for pathological tissues are rather independent of the structure and content of the image (e.g., the shape and location of lesions), it is likely the outputs of a network trained to represent the local relationship can preserve the sensitivity of FA difference between normal and

pathological tissues.

It is worth noting that the fiber tractography obtained in this study is equivalent to that obtained from the convention DTI. Therefore, the method is not able to resolve fiber crossing. More DWIs from more diffusion directions are necessary to perform fiber tracking with the capability of resolving crossing fibers (26). Since DTI-derived tractography has demonstrated clinical relevance (51,52), this study is to enable superfast tractography in clinical settings.

Based on the mathematical model of diffusion imaging (50), the network should only depend on the diffusion gradients applied. If the diffusion gradients and the contrasts are the same, the trained model should be applicable to future datasets (e.g., with different SNR, pathological information, etc.) acquired on the same MRI systems. However, imperfections (e.g., noise and artifacts) during the acquisition can cause the network to be dependent on other factors such as field strength and coils. The effects of various factors will be explored in our future studies.

## **6. CONCLUSION**

In this paper, we demonstrated the feasibility of superfast diffusion tensor imaging and fiber tractography using SuperDTI with only six DWIs (that could be noisy and corrupted by artifacts). The proposed SuperDTI outperformed the conventional tensor model fitting and other state-of-the-art methods using both qualitative and quantitative metrics. We also demonstrated that the neural network trained on healthy volunteer datasets could be directly applied to stroke patient's data without compromising the lesion detectability, and the network trained using clean DWIs could be applied to noisy DWIs with high FA accuracy. In summary, the proposed SuperDTI is expected to benefit a wide range of clinical and neuroscientific studies that require superfast but reliable DTI.

## ACKNOWLEDGMENTS

This work is supported in part by the National Institute of Health Brain Initiative R01EB025133.

## REFERENCE

1. Moseley ME, Cohen Y, Mintorovitch J, Chileuitt L, Shimizu H, Kucharczyk J, Wendland M, Weinstein P. Early detection of regional cerebral ischemia in cats: comparison of diffusion - and T2 - weighted MRI and spectroscopy. *Magnetic resonance in medicine* 1990;14(2):330-346.
2. Le Bihan D. Molecular diffusion nuclear magnetic resonance imaging. *Magnetic resonance quarterly* 1991;7(1):1.
3. Bammer R. Basic principles of diffusion-weighted imaging. *European journal of radiology* 2003;45(3):169-184.
4. Lansberg MG, Norbash AM, Marks MP, Tong DC, Moseley ME, Albers GW. Advantages of adding diffusion-weighted magnetic resonance imaging to conventional magnetic resonance imaging for evaluating acute stroke. *Archives of neurology* 2000;57(9):1311-1316.
5. Larsson H, Thomsen C, Frederiksen J, Stubgaard M, Henriksen O. In vivo magnetic resonance diffusion measurement in the brain of patients with multiple sclerosis. *Magnetic resonance imaging* 1992;10(1):7-12.
6. Christiansen P, Gideon P, Thomsen C, Stubgaard M, Henriksen O, Larsson H. Increased water self - diffusion in chronic plaques and in apparently normal white matter in patients with multiple sclerosis. *Acta neurologica scandinavica* 1993;87(3):195-199.
7. Horsfield MA, Lai M, Webb SL, Barker GJ, Tofts PS, Turner R, Rudge P, Miller DH. Apparent diffusion coefficients in benign and secondary progressive multiple sclerosis by nuclear magnetic resonance. *Magnetic resonance in medicine* 1996;36(3):393-400.
8. Nakahara M, Ericson K, Bellander B. Diffusion-weighted MR and apparent diffusion coefficient in the evaluation of severe brain injury. *Acta Radiologica* 2001;42(4):365-369.
9. Sundgren P, Reinstrup P, Romner B, Holtås S, Maly P. Value of conventional, and diffusion-and perfusion weighted MRI in the management of patients with unclear cerebral pathology, admitted to the intensive care unit. *Neuroradiology* 2002;44(8):674-680.
10. Kono K, Inoue Y, Nakayama K, Shakudo M, Morino M, Ohata K, Wakasa K, Yamada R. The role of diffusion-weighted imaging in patients with brain tumors. *American journal of neuroradiology* 2001;22(6):1081-1088.
11. Stadnik TW, Chaskis C, Michotte A, Shabana WM, Van Rompaey K, Luypaert R, Budinsky L, Jellus V, Osteaux M. Diffusion-weighted MR imaging of intracerebral masses: comparison with conventional MR imaging and histologic findings. *American journal of neuroradiology* 2001;22(5):969-976.
12. Hinchey J, Chaves C, Appignani B, Breen J, Pao L, Wang A, Pessin MS, Lamy C, Mas J-L, Caplan LR. A reversible posterior leukoencephalopathy syndrome. *New England Journal of Medicine* 1996;334(8):494-500.
13. Sundgren P, Edvardsson B, Holtås S. Serial investigation of perfusion disturbances and vasogenic oedema in hypertensive encephalopathy by diffusion and perfusion weighted imaging.

Neuroradiology 2002;44(4):299-304.

14. Basser PJ, Mattiello J, LeBihan D. Estimation of the effective self-diffusion tensor from the NMR spin echo. *Journal of Magnetic Resonance, Series B* 1994;103(3):247-254.
15. Krissian K, Malandain G, Ayache N. Directional anisotropic diffusion applied to segmentation of vessels in 3D images. 1997. Springer. p 345-348.
16. Lu H, Jensen JH, Ramani A, Helpert JA. Three - dimensional characterization of non - gaussian water diffusion in humans using diffusion kurtosis imaging. *NMR in Biomedicine: An International Journal Devoted to the Development and Application of Magnetic Resonance In vivo* 2006;19(2):236-247.
17. Tuch DS, Reese TG, Wiegell MR, Makris N, Belliveau JW, Wedeen VJ. High angular resolution diffusion imaging reveals intravoxel white matter fiber heterogeneity. *Magnetic Resonance in Medicine: An Official Journal of the International Society for Magnetic Resonance in Medicine* 2002;48(4):577-582.
18. Barth M, Breuer F, Koopmans PJ, Norris DG, Poser BA. Simultaneous multislice (SMS) imaging techniques. *Magnetic resonance in medicine* 2016;75(1):63-81.
19. Landman BA, Wan H, Bogovic JA, Bazin P-L, Prince JL. Resolution of crossing fibers with constrained compressed sensing using traditional diffusion tensor MRI. 2010. *International Society for Optics and Photonics*. p 76231H.
20. Menzel MI, Tan ET, Khare K, Sperl JI, King KF, Tao X, Hardy CJ, Marinelli L. Accelerated diffusion spectrum imaging in the human brain using compressed sensing. *Magnetic Resonance in Medicine* 2011;66(5):1226-1233.
21. Michailovich O, Rathi Y, Dolui S. Spatially regularized compressed sensing for high angular resolution diffusion imaging. *IEEE transactions on medical imaging* 2011;30(5):1100-1115.
22. Landman BA, Bogovic JA, Wan H, ElShahaby FEZ, Bazin P-L, Prince JL. Resolution of crossing fibers with constrained compressed sensing using diffusion tensor MRI. *NeuroImage* 2012;59(3):2175-2186.
23. Wu Y, Zhu YJ, Tang QY, Zou C, Liu W, Dai RB, Liu X, Wu EX, Ying L, Liang D. Accelerated MR diffusion tensor imaging using distributed compressed sensing. *Magnetic resonance in medicine* 2014;71(2):763-772.
24. Shi X, Ma X, Wu W, Huang F, Yuan C, Guo H. Parallel imaging and compressed sensing combined framework for accelerating high - resolution diffusion tensor imaging using inter - image correlation. *Magnetic resonance in medicine* 2015;73(5):1775-1785.
25. Golkov V, Dosovitskiy A, Sperl JI, Menzel MI, Czisch M, Sämann P, Brox T, Cremers D. q-Space deep learning: twelve-fold shorter and model-free diffusion MRI scans. *IEEE transactions on medical imaging* 2016;35(5):1344-1351.
26. Lin Z, Gong T, Wang K, Li Z, He H, Tong Q, Yu F, Zhong J. Fast learning of fiber orientation distribution function for MR tractography using convolutional neural network. *Medical physics* 2019;46(7):3101-3116.
27. Poulin P, Cote M-A, Houde J-C, Petit L, Neher PF, Maier-Hein KH, Larochelle H, Descoteaux M. Learn to track: Deep learning for tractography. 2017. Springer. p 540-547.
28. Gong T, He H, Li Z, Lin Z, Tong Q, Li C. Efficient reconstruction of diffusion kurtosis imaging based on a hierarchical convolutional neural network. 2018. p 1653.
29. Li H, Zhang C, Liang Z, Shen B, Ge Y, Zhang J, Liu R, Huang P, Gaire SK, Ying L. Deep learning diffusion tensor imaging with accelerated q-space acquisition. 2018; District of Columbia,

Washington. USA.

30. Li H, Zhang C, Liang Z, Shen B, Ge Y, Zhang J, Liu R, Huang P, Gaire SK, Zhang X, Ying L. Deep Learned Diffusion Tensor Imaging. 2019; Montreal, Canada.
31. Aliotta E, Nourzadeh H, Sanders J, Muller D, Ennis DB. Highly accelerated, model - free diffusion tensor MRI reconstruction using neural networks. *Medical physics* 2019;46(4):1581-1591.
32. Gibbons EK, Hodgson KK, Chaudhari AS, Richards LG, Majersik JJ, Adluru G, DiBella EV. Simultaneous NODDI and GFA parameter map generation from subsampled q - space imaging using deep learning. *Magnetic resonance in medicine* 2019;81(4):2399-2411.
33. Li Z, Gong T, Lin Z, He H, Tong Q, Li C, Sun Y, Yu F, Zhong J. Fast and robust diffusion kurtosis parametric mapping using a three-dimensional convolutional neural network. *IEEE Access* 2019;7:71398-71411.
34. Tian Q, Bilgic B, Fan Q, Liao C, Ngamsombat C, Hu Y, Witzel T, Setsompop K, Polimeni JR, Huang SY. DeepDTI: High-fidelity six-direction diffusion tensor imaging using deep learning. *NeuroImage* 2020:117017.
35. Ronneberger O, Fischer P, Brox T. U-net: Convolutional networks for biomedical image segmentation. 2015. Springer. p 234-241.
36. He K, Zhang X, Ren S, Sun J. Deep residual learning for image recognition. 2016. p 770-778.
37. Kim J, Kwon Lee J, Mu Lee K. Accurate image super-resolution using very deep convolutional networks. 2016. p 1646-1654.
38. Dong C, Loy CC, He K, Tang X. Image super-resolution using deep convolutional networks. *IEEE transactions on pattern analysis and machine intelligence* 2015;38(2):295-307.
39. Jia Y, Shelhamer E, Donahue J, Karayev S, Long J, Girshick R, Guadarrama S, Darrell T. Caffe: Convolutional architecture for fast feature embedding. 2014. ACM. p 675-678.
40. Van Essen DC, Ugurbil K, Auerbach E, Barch D, Behrens T, Bucholz R, Chang A, Chen L, Corbetta M, Curtiss SW. The Human Connectome Project: a data acquisition perspective. *Neuroimage* 2012;62(4):2222-2231.
41. Li J, Zhang XW, Zuo ZT, Lu J, Meng CL, Fang HY, Xue R, Fan Y, Guan YZ, Zhang WH. Cerebral functional reorganization in ischemic stroke after repetitive transcranial magnetic stimulation: an fMRI study. *CNS neuroscience & therapeutics* 2016;22(12):952-960.
42. Guan YZ, Li J, Zhang XW, Wu S, Du H, Cui LY, Zhang WH. Effectiveness of repetitive transcranial magnetic stimulation (rTMS) after acute stroke: A one - year longitudinal randomized trial. *CNS neuroscience & therapeutics* 2017;23(12):940-946.
43. Skare S, Hedehus M, Moseley ME, Li T-Q. Condition number as a measure of noise performance of diffusion tensor data acquisition schemes with MRI. *Journal of magnetic resonance* 2000;147(2):340-352.
44. Tournier JD, Calamante F, Connelly A. MRtrix: diffusion tractography in crossing fiber regions. *International journal of imaging systems and technology* 2012;22(1):53-66.
45. Dabov K, Foi A, Katkovnik V, Egiazarian K. Image denoising by sparse 3-D transform-domain collaborative filtering. *IEEE Transactions on image processing* 2007;16(8):2080-2095.
46. Maggioni M, Katkovnik V, Egiazarian K, Foi A. Nonlocal transform-domain filter for volumetric data denoising and reconstruction. *IEEE transactions on image processing* 2012;22(1):119-133.
47. Jiang H, Van Zijl PC, Kim J, Pearlson GD, Mori S. DtiStudio: resource program for diffusion

tensor computation and fiber bundle tracking. *Computer methods and programs in biomedicine* 2006;81(2):106-116.

48. Liang Z, He X, Ceritoglu C, Tang X, Li Y, Kuttan KS, Oishi K, Miller MI, Mori S, Faria AV. Evaluation of cross-protocol stability of a fully automated brain multi-atlas parcellation tool. *PloS one* 2015;10(7):e0133533.

49. Wang Z, Bovik AC, Sheikh HR, Simoncelli EP. Image quality assessment: from error visibility to structural similarity. *IEEE transactions on image processing* 2004;13(4):600-612.

50. Kiselev VG. The cumulant expansion: an overarching mathematical framework for understanding diffusion NMR. *Diffusion MRI: theory, methods, and applications* 2010:152-168.

51. Bello L, Gambini A, Castellano A, Carrabba G, Acerbi F, Fava E, Giussani C, Cadioli M, Blasi V, Casarotti A. Motor and language DTI Fiber Tracking combined with intraoperative subcortical mapping for surgical removal of gliomas. *Neuroimage* 2008;39(1):369-382.

52. Giussani C, Poliakov A, Ferri RT, Plawner LL, Browd SR, Shaw DW, Filardi TZ, Hoepfner C, Geyer JR, Olson JM. DTI fiber tracking to differentiate demyelinating diseases from diffuse brain stem glioma. *Neuroimage* 2010;52(1):217-223.